# Supplementary Information

# Ubiquitous karst hydrological control on speleothem oxygen isotopic variability in a global study


# Treble P.C. et al.


The Supplementary Information comprises:

**Supplementary Notes**



**Supplementary Tables**



**Supplementary Figures**



**Supplementary references**

**Supplementary Notes**

Supplementary Note 1: Farmed calcites and conversion of dripwater $\delta^{18}O$ to calcite equivalent values.

Two substrate types were used to collect modern calcite ('farmed calcites') that formed contemporaneously with the dripwater monitoring. Prior to 2013 these were discs machined from Delrin® plastic rod with approximate dimensions of 25 mm diameter and 4 mm thickness and sand-blasted to increase surface roughness and promote calcite precipitation. Following the introduction of acoustic drip loggers into each funnel, the substrate was switched to inverted watch glasses with roughened convex surface that could be placed on top of the logger and still permit acoustic transmission. Approximately 25-50 µg of carbonate was scraped from the substrates directly into the reaction thimbles. This was repeated to reproduce duplicate or triplicate measurements where possible and an average calculated (Table 1). Samples were measured on the MAT-253 isotope ratio mass spectrometer with Kiel carbonate device at the Mark Wainwright Analytical Centre at UNSW Sydney according to the method in ref[1]. Data are normalised to the Vienna Pee Dee Belemnite (VPDB) scale using NBS19 ($\delta^{18}O$=−2.20‰ and $\delta^{13}C$=+1.95‰) and NBS-18 ($\delta^{18}O$=−23.0‰ and $\delta^{13}C$=−5.0‰). Analytical precision for the analyses reported here (NBS-19) are ±0.04 ‰ for $\delta^{18}O$ and ±0.04 ‰ for $\delta^{13}C$ (N=4). An isotopic fractionation factor ($\alpha_{calcite\text{-}water}$) was calculated using the equation:

$$\alpha_{calcite-water} = \frac{1 + \frac{\delta_{calcite}}{1000}}{1 + \frac{\delta_{water}}{1000}}$$

where $\delta_{calcite}$ is the farmed calcite $\delta^{18}O$ and $\delta_{water}$ is the corresponding mean drip water $\delta^{18}O$ value over the corresponding period each substrate was in the cave. $\delta_{water}$ is converted to the equivalent value on the VPDB scale using the equation $\delta^{18}O_{VPDB} = 0.97001 * \delta^{18}O_{VSMOW} - 29.99$.

Dripwater $\delta^{18}O$ measurements were converted from the VSMOW scale to a calcite equivalent on the VPDB scale using the average calculated isotopic fractionation factor (1.03185 ± 0.00013) and mean monthly cave temperature measured at Golgotha Cave (14.6±0.1°C; May 2017-July 2020).

Supplementary Note 2: Assessment of disequilibrium and/or kinetics on speleothem $\delta^{18}O$

Speleothem fabrics determined from thin section analysis shows that all stalagmites are columnar and open-columnar fabrics (see for fabric descriptions ref[2]) with no fabrics associated with "disequilibrium deposition" such as dendritic, micrite, microsparitic fabrics, detected.

Disequilibrium and/or kinetic isotopic effects result in a $\alpha_{calcite\text{-}water}$ value that departs from a value determined under conditions of thermodynamic equilibrium. Table 1 (main paper) shows that the $\alpha_{calcite\text{-}water}$ values calculated from our farmed calcites are consistent across the monitored Golgotha Cave drip sites (1.03185±0.00013) and the range in measured $1000\ln\alpha_{calcite\text{-}water}$ values between sites is 0.3‰. This is regardless of differences in drip rate. This demonstrates that disequilibrium and/or kinetic isotopic effects are not responsible for the difference in farmed calcites values over the monitored interval and we infer not responsible for the differences in mean speleothem $\delta^{18}O$. Rather, the difference in mean speleothem $\delta^{18}O$ values for Golgotha Cave are dominated by the difference in dripwater $\delta^{18}O$ values and this is driven by the ratio of matrix to fracture flow along a flowpath. Possible exceptions to this, as raised in the main text, are the interval 1300-1380 CE in GL-S3. We investigate this further below by investigating the relationship between speleothem $\delta^{13}C$ versus $\delta^{18}O$ which has been used as a possible diagnostic of disequilibrium and/or kinetic isotopic effects[3].

Scatterplots for Golgotha speleothems are shown in Supplementary Figure 3. Speleothem growth with lowest slope values and least co-variation between $\delta^{13}C$ and $\delta^{18}O$ occurs when $\delta^{18}O$ values are lowest, i.e., during times of persistent fracture flow in these speleothem records (e.g., 1180-1300 CE for GL-S3 and 1580-1790 CE GL-S4; see main text). Highest slope and co-variation are observed for speleothem GL-S3 during 1300-1380 CE when GL-S3 $\delta^{18}O$ values rapidly rise and exceed neighbouring matrix flow speleothems by at least 1 ‰. As outlined in the main text, this isotopic maximum precedes a growth hiatus and is interpreted to represent processes that could occur once a karst store is disconnected from infiltration and subsequently drains. This could include enhanced disequilibrium and/or kinetic isotopic fractionation between speleothem calcite and its source water as the drip interval lengthens. From 1180 to 1260 CE, GL-S1 and GL-S4 have high, declining $\delta^{18}O$ values (Fig. 4a; main text) as well as high slope and $r^2$ values (Supplementary Figure 3b). Prior to this, GL-S1 sustained mean $\delta^{18}O$ value of -2.6±0.3‰ for a multi-centennial period. Regardless of the driver of these GL-S1 $\delta^{18}O$ values during this period, the high value as well as lack of growth in the other three stalagmites supports an extended dry period. This indicates that the downward trending

values for GL-S1 and GL-S4 prior to 1200 CE are likely associated with establishment of new or reliable water percolation along a flow path. Thus the high values prior to 1200 CE and the high slope and $r^2$ values could indicate enhanced disequilibrium and or kinetic isotope fractionation due to very low drip rates or the incorporation of older water with high $\delta^{18}O$ values as a result of having been disconnected from infiltration during a dry period. Speleothems that are dominated by matrix flow either because they lack a fracture flow path (GL-S1) or during periods when the ratio of fracture to matrix flow is reduced (e.g. 1260-1580 GL-S4) have intermediate slope and $r^2$ values (Supplementary Figure 3). Speleothems have different mean $\delta^{13}C$ values (Supplementary Fig. 3c) supporting mean speleothem $\delta^{13}C$ is also related to speleothems being fed by different flowpaths. Furthermore, speleothem $\delta^{13}C$ is smoothly varying through time (Supplementary Fig. 3c) supporting an environmental not disequilibrium or kinetic control. Combining observations that variability in speleothem $\delta^{18}O$ values are driven by fracture activation and that the strength of the relationship between speleothem $\delta^{18}O$ and $\delta^{13}C$ also varies according to flow type, raises the likely possibility that dripwater $\delta^{13}C$ may also be influenced by individual flow paths, with the possible exception of when dripwater becomes disconnected from infiltration.

Supplementary Note 3: Assessment of evaporation on dripwater $\delta^{18}O$

The range of mean dripwater $\delta^{18}O$ values accounts for the range in mean speleothem $\delta^{18}O$ values indicating that the differences between Golgotha Cave speleothems is primarily driven by dripwater $\delta^{18}O$. Our long-term monitoring demonstrates that the isotopic differences between flowpaths is attributable to the balance between matrix and fracture flow for each flowpath. Treble et al. (2013) ruled out the impact of evaporation within the karst as a driver of dripwater $\delta^{18}O$ as the dripwater $\delta^{18}O$ values are the same or lower than incoming rainfall. Here, we further address the alternative hypothesis that evaporation of water on stalactites could account for higher dripwater $\delta^{18}O$ at our slower dripping sites by examining relative humidity and pan evaporation data from Golgotha Cave. Average monthly relative humidity values were calculated from data originally acquired at 15 min intervals using a Datataker DT80 logger between May 2017 and July 2020 using a Vaisala HMP155 with Humicap 180RC and sensor warming enabled to negate saturation of the sensor at high humidity (accuracy $\pm$1.8%). High relative humidity is maintained throughout the year with an average of 98.9% (range 95.7 to 100%). Evaporation pans consisting of 95 mm diameter petri dishes glasses in triplicate were placed near our dripwater monitoring site in chamber 1 over two years (May 2012 – March 2014). Pans were filled with 70 mls of tapwater using a measuring cylinder. The volume of water lost was measured every six weeks when the pans were emptied and refilled. The average evaporation rate was 0.009 mm day$^{-1}$ (range 0.002 to 0.019 mm day$^{-1;}$ n=13).

We modelled the isotopic impact of evaporation on a thin film assuming a worse-case scenario whereby water flows exclusively on the outer surface of a stalactite and an evaporation rate of 0.1 mm day$^{-1}$. Assuming a drip volume, $V_d = 0.2$ mL, the water flux is

$$Q = \frac{V_d}{\tau}$$

where $\tau$ is the interval between drips. The evaporation rate inside the cave, $E = 0.1$mm/day, so the evaporation flux from water film over the stalagmite is

$$Q_E = EA_f$$

where $A_f$ is the surface area of the film. Assuming that $Q_E \ll Q$, so that $Q + Q_E \approx Q$, the fraction of water which remains in the liquid phase is

$$f_l = 1 - \frac{Q_E}{Q}.$$

Modelling the stalactite as a cylinder with length 6 cm and diameter 1 cm, based on measurements of stalactites at this site[4], and assuming $\tau = 300s$ we obtain

$$f_l = 99.67\%.$$

To calculate isotopic fractionation, we assume that kinetic fractionation can be neglected because of the high humidity of the cave. With this condition, the result from Rayleigh Fractionation applies[5] which, for this system where vapour is removed, is written

$$R = R_0 f_l^{1/\alpha - 1}$$

where $\alpha$ is the equilibrium fraction factor, $\alpha = 1.0101$ at 16°C[6], $R$ is the ratio of heavy-to-light isotopes, and $R_0$ is the initial $R$ of the infiltrating water. Setting $R_0$ to equal standard VSMOW, using $f_l = 99.67$ calculated above, and converting to $\delta$ notation,

$$\delta_l = 0.03‰.$$

Thus, assuming a worse-case scenario of evaporation that is 5x higher than our observed value results in an estimated increase in dripwater $\delta^{18}O$ of 0.03‰, that is too weak by a factor of >10 to explain drip $\delta^{18}O$ variability.

**Supplementary Table 1:** Summary of method used for analysis of SISALv2 data and statistics (first entry) compared with other possible methods. N is the number of cases of coeval records. The average speleothem $\Delta\delta^{18}O_{means}$ was statistically insignificant from the other methods, the interquartile range was very similar, as were the % of coeval records where $\Delta\delta^{18}O_{means}$ >0.3 ‰. That is, the impact of unevenly versus evenly sampled data, considering the record as a whole versus splitting into sub-records according to hiatuses and/or varying the criteria for the duration of the overlap interval had no overall impact on our interpretation. As such, we chose to report the statistics using the first method as it involved the least processing of the original data as it appears in SISALv2.

| | Global average $\Delta\delta^{18}O_{means}$ (‰$_{VPDB}$) | | | | | | | % of coeval records $\Delta\delta^{18}O_{means}$ >0.3 ‰ |
|---|---|---|---|---|---|---|---|---|
| Criteria | N | Average | Standard deviation | 1st quartile | 2nd quartile | 3rd quartile | Inter-quartile range | |
| Method used: 'mineralogy' = calcite AND coeval interval exceeds 10% of the minimum age of overlap AND overlap interval exceeds 2x'lin_interp_age_uncert_pos' of the maximum age AND 2x'lin_interp_age_uncert_neg' of the minimum age AND each section contain >10 $\delta^{18}O$ measurements. | 146 | 0.37 | 0.33 | 0.15 | 0.27 | 0.51 | 0.36 | 45 |
| Variations to above criteria: | | | | | | | | |
| Speleothem with higher number of $\delta^{18}O$ measurements was interpolated to be equivalently sampled as the lower resolution record over the period of coeval growth | 146 | 0.34 | 0.33 | 0.11 | 0.24 | 0.47 | 0.36 | 41 |
| Records treated separate coeval records if a hiatus within the coeval interval was detected | 190 | 0.35 | 0.37 | 0.11 | 0.23 | 0.45 | 0.34 | 38 |
| 5 % overlap in coeval age interval | 178 | 0.36 | 0.32 | 0.13 | 0.26 | 0.52 | 0.39 | 43 |

**Supplementary Table 2:** Multiple linear regression model (MLR) output for dripwater and for SISALv2 speleothem datasets for climate variables or variables sensitive to climate (latitude and elevation). The p-values indicate that none of the relationships in the MLR models are significant and the $r^2$ values are low. These results indicate that the within-cave variability in mean dripwater and mean speleothem $\delta^{18}O$ values are not related to climate or the other variables considered. This further suggests that karst hydrological heterogeneity is important over all climate types, cave depths and host rock types. The MLR is represented as $y=(a_1\pm\sigma_1)x_1 + (a_2\pm\sigma_2)x_2 + \ldots + (a_n\pm\sigma_n)x_n + (b\pm\sigma)$ for variables 1 to n. The engineering notation used in the MLR output is base 10 e.g. -2.06E-03 is equivalent to $-2.06\times10^{-3}$. The MLR analysis shown here was calculated using an average of the $\Delta\delta^{18}O_{means}$ value for each cave (N=64). The MLR analysis was repeated using all cases of coeval speleothem $\Delta\delta^{18}O_{means}$ data (N=146) and the $r^2$ value was 0.05.

| | Coefficient (a) | Standard error (σ) | p-value |
|---|---|---|---|
| Dripwater ($r^2$ = 0.09) | | | |
| Latitude | -2.06E-03 | 2.75E-02 | 0.46 |
| Elevation | -1.98E-04 | 2.06E-04 | 0.92 |
| Mean ann. temperature | 2.49E-03 | 2.20E-02 | 0.91 |
| Precipitation | 1.65E-4 | 2.66E-04 | 0.54 |
| Aridity index | -3.26E-01 | 2.49E-01 | 0.20 |
| Seasonality index, temperature | -4.59E-06 | 4.96E-05 | 0.93 |
| Seasonality index, precipitation | -1.73E-03 | 3.07E-03 | 0.58 |
| Intercept (b) | 7.60E-01 | 5.40E-01 | 0.17 |
| Speleothem ($r^2$ = 0.14) | | | |
| Latitude | -2.56E-03 | 2.18E-03 | 0.24 |
| Elevation | -7.86E-05 | 5.78E-05 | 0.18 |
| Mean ann. temperature | 5.50E-03 | 1.42E-02 | 0.70 |
| Precipitation | -6.60E-06 | 9.01E-05 | 0.94 |
| Aridity index | 4.25E-02 | 9.51E-02 | 0.66 |
| Seasonality index, temperature | 3.57E-05 | 2.53E-05 | 0.16 |
| Seasonality index, precipitation | 6.16E-04 | 1.34E-03 | 0.65 |
| Intercept (b) | -2.56E-03 | 2.18E-03 | 0.24 |

**Supplementary Table 3:** Description of paired drip sites and stalagmites. Further detail on flow types and drip rate data are given in ref.[4,7]. Images of the stalagmites are given in Supplementary Figure 2.

| Drip ID | Flow type | Stalagmite ID | Stalagmite description |
|---|---|---|---|
| Site 1A | Predominately matrix | GL-S1 | Near-uniform diameter candle-stick type stalagmite, indicating consistency in drip rate through time, from chamber 1. White, open columnar fabric during last millennium growth section; closed columnar fabric in preceding growth. |
| Site 1IV | Matrix plus fracture | GL-S4 | Uniform diameter candle-stick type stalagmite from chamber 1. White, open columnar fabric. |
| Site 2B | Matrix plus underflow from secondary store (see also ref[8]) | GL-S2 | Approximately uniform width boss-type stalagmite from chamber 2. Gour features on sides indicative of faster flow during past. Closed, columnar fabric. |
| Site 2E | Combination | GL-S3 | Irregular width boss-type stalagmite from chamber 2. Gour features on sides indicative of faster flow during past. Closed, columnar fabric. |

**Supplementary Table 4:** Summary of techniques used to construct chronologies for Golgotha Cave speleothems. Data from bomb pulse model previously published in ref.[9]. ADM is age-depth model (Supplementary Figure 4). U/Th age measurements are in Supplementary Data 5.

| Speleothem | Growth interval (CE)* | Comment |
|---|---|---|
| GL-S1 | 1920-2005: bomb pulse ADM and year of collection (2005).<br>1000-1920: U/Th age ADM (17$^{th}$ percentile used) | In Figure S4, the 17$^{th}$ percentile, rather than the median, ADM is used to align $\delta^{18}O$ maxima with the laminae counted GL-S4 $\delta^{18}O$ record. This shifts the record 45 years younger at the oldest end of the record shown. See Supplementary Figure 5. |
| GL-S2 | 1330-2005: Combined ADM using laminae count scaled to two tie-points (1950 CE in the bomb pulse ADM and the year of collection 2005) and U/Th ages measurements. | Hiatus at 32.6 mm determined from visible feature and bracketing age measurements. Laminae count based on a Sr line scan extracted from synchrotron XFM created for 0-13.6 mm. The Sr laminae were visible in the XFM image for GL-S2 but of insufficient clarity to confidently visualise growth laminae across the width of the map owing to the 'fuzzy' appearance of the bands. Thus the laminae count was based on three 'line scans' extracted from the map using ImageJ and counting the common peaks in Sr across the three lines rather than the preferred method of counting the Sr laminae by detection of continuous laminae features across the map. As a chross-check the laminae count was compared to the bomb pulse ADM and as a result scaled to 88(±12)%. This is consistent with the tendency for more 'false' Sr peaks to be encounted in line scans versus the 2D map. |
| GL-S3 | 1950-2008: mean laminae growth rate (69±11 µm/a; laminae were present for 27% of growth) and year of collection (2008).<br>1180-1380: Combined U/Th ADM and laminae counting. | Hiatus at 4.2 mm depth determined from visible feature. Lack of deposition below 1180 CE determined from bracketing radiometric ages and visible hiatus at 21.5 mm depth. Linear extrapolation of growth rate between 17-20 mm was applied to extend the ADM from 20 to 21.5 mm. |
| GL-S4 | 1200-2012: Sr laminae counting and year of collection. Laminae ADM published in ref[10]. | Laminae chronology is supported by both bomb pulse ADM and U/Th ages. Hiatus at 46.4 mm indicated by detrital layer and supported by bracketing ages. |

*Median ages used unless stated: see Supplementary Figure 4 for ADM uncertainties.

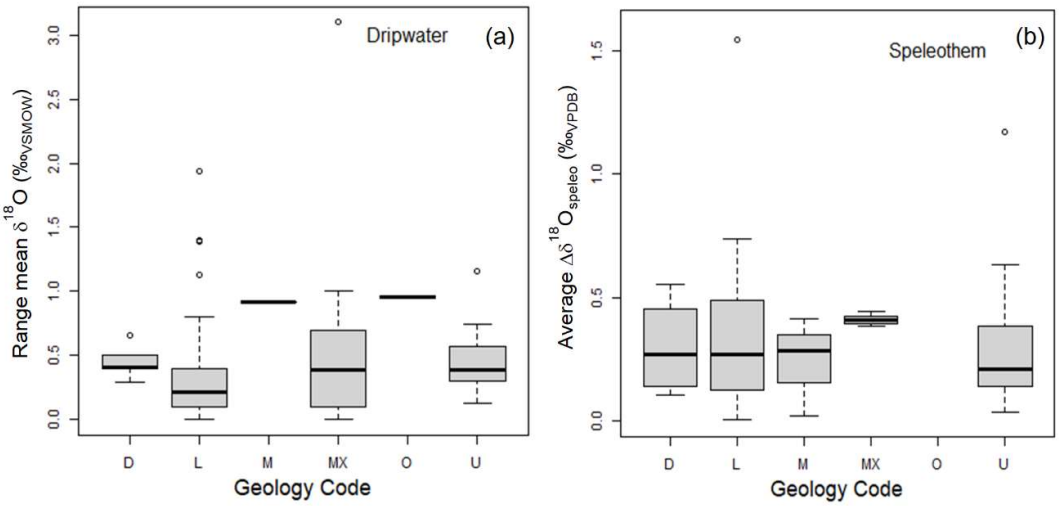


**Supplementary Figure 1a,b:** Mann-Whitney U test for within-cave range in mean $\delta^{18}O$ values for dripwater and geology type (a), and for average speleothem $\Delta\delta^{18}O_{means}$ and geology type (b). Geology codes: D is dolomite, L is limestone, M is marble, MX is mixed, O is 'other' and U is unknown. There were no significant differences in median values for different host rock types using a p-value = 0.05 for either the dripwater or speleothem datasets. For dripwaters, the differences significant at p-value = 0.1 between dolomite and 'other' although 'other' had a small number of values; and between limestone and 'unknown' although there is an overlap of the distributions.

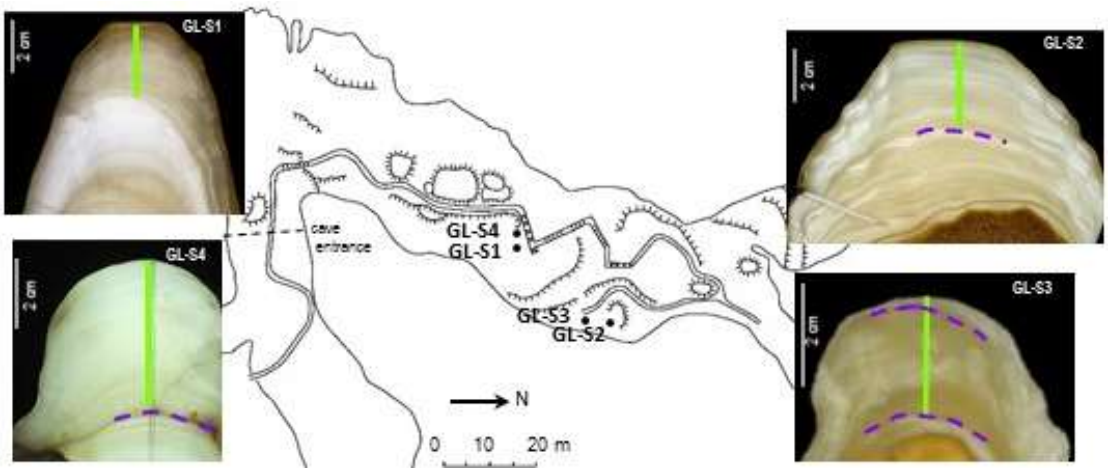


**Supplementary Figure 2**: Plan view of Golgotha Cave and images of four speleothems used in this study. The drip logger network referred to in the main text are clusterd at the GL-S1/GL-S4 and the GL-S2/GL-S3 sites. See ref.[7] for detailed maps showing individual locations of the data loggers. Green lines on images indicates milled transect of $\delta^{18}O$ data and purple dashed line indicates location of growth hiatuses. Golgotha Cave experiences dry summers and wet winters from the seasonal migration of the mid-latitude westerly winds. Mean annual rainfall is 1136 mm, recorded at the Bureau of Meterology station 9547 (Forest Grove, 5 km from Golgotha Cave; average is for all years station has operated, 1925-present). Precipitation falls as rain only. Golgotha Cave temperature is 14.6±0.1°C. The surface vegetation is wet eucalypt forest growing in a soil comprised of weathered siliceous dune sands. Golgotha Cave is developed in Quaternary aeolinite ('Tamala Limestone') and the thickness between the surface and the ceiling above the sampling sites is approximately 32 m. See refs.[7-8] for further details on the site description.

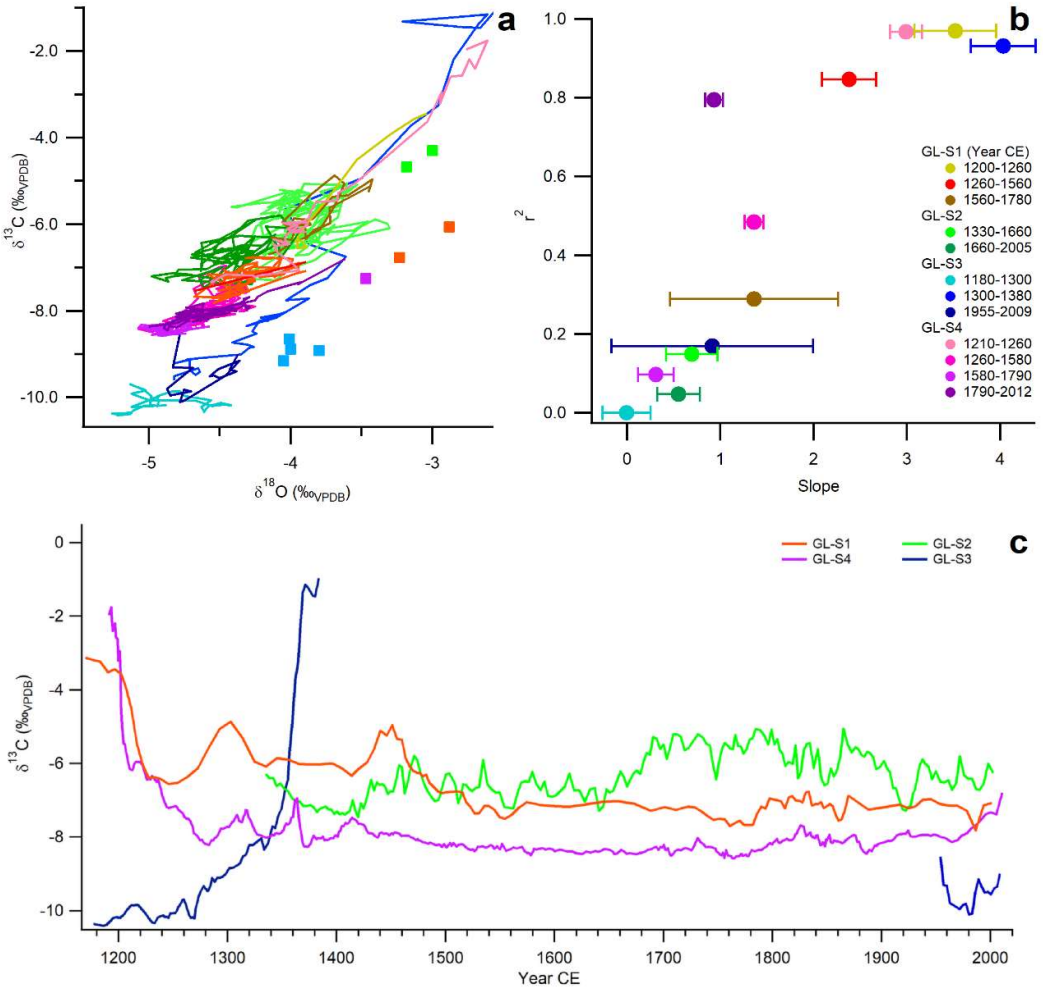


**Supplementary Figure 3a-c.** Scatterplots of speleothem $\delta^{13}C$ versus $\delta^{18}O$ for Golgotha speleothems (a); Pearson's $r^2$ value versus slope for intervals chosen from panel a with different slope and $r^2$ values (b); and $\delta^{13}C$ time series (c). Farmed calcites (square symbols) also appear on (a) for comparison. Colour-coding on legend on (b) applies to both plots. Error bars on (b) indicate the 95% confidence interval of the fit for the coefficient (slope) value. Intervals with lowest $\delta^{18}O$ values (highest fracture flow influence) have weakest relationships between speleothem $\delta^{13}C$ and $\delta^{18}O$ values.

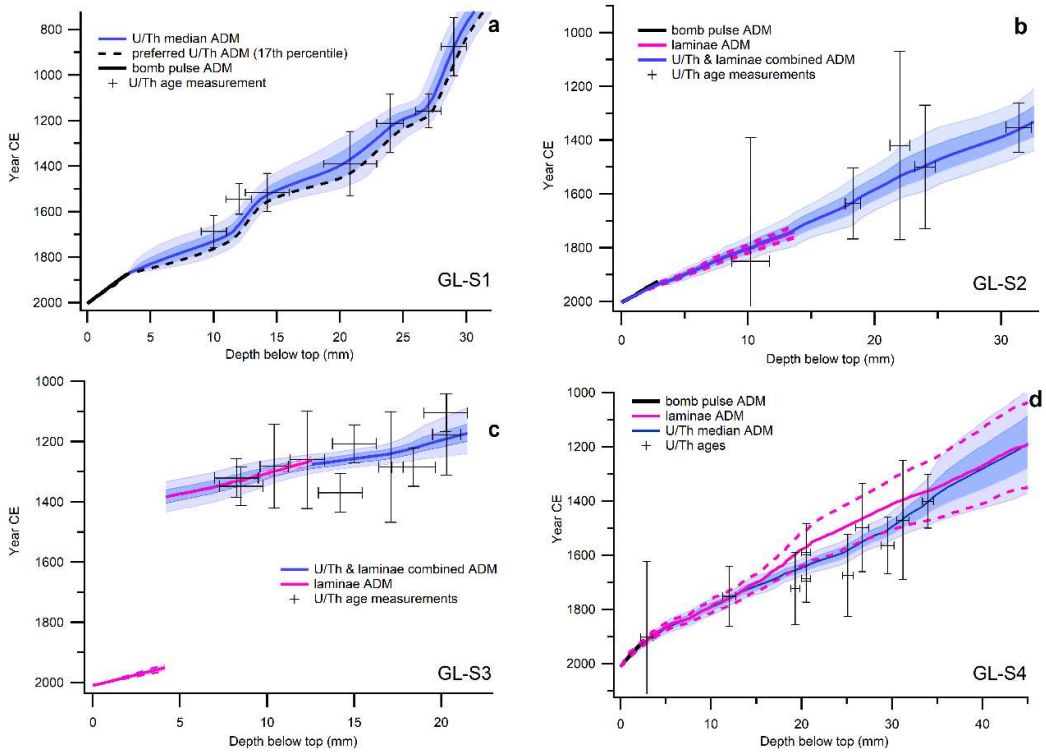


**Supplementary Figure 4a-d**. Age-depth models for each stalagmite based on U/Th age measurements and bomb pulse models for stalagmites GL-S1 (a), GL-S2 (b), GL-S3 (c) and GL-S4 (d). Also shown are age-depth models derived from Sr concentration laminae and bomb pulse ADM. See Supplementary Table 4 for further details on the chronologies. Error bars on U/Th ages are ±2$\sigma$ uncertainties. Darker blue shading on age-depth model indicates the 17$^{th}$ and 83$^{rd}$ confidence interval and the lighter blue shading, the 3$^{rd}$ and the 97$^{th}$ confidence interval. Uncertainty on bomb pulse ADM is +/-0.05 mm and +/-0.004 ka.

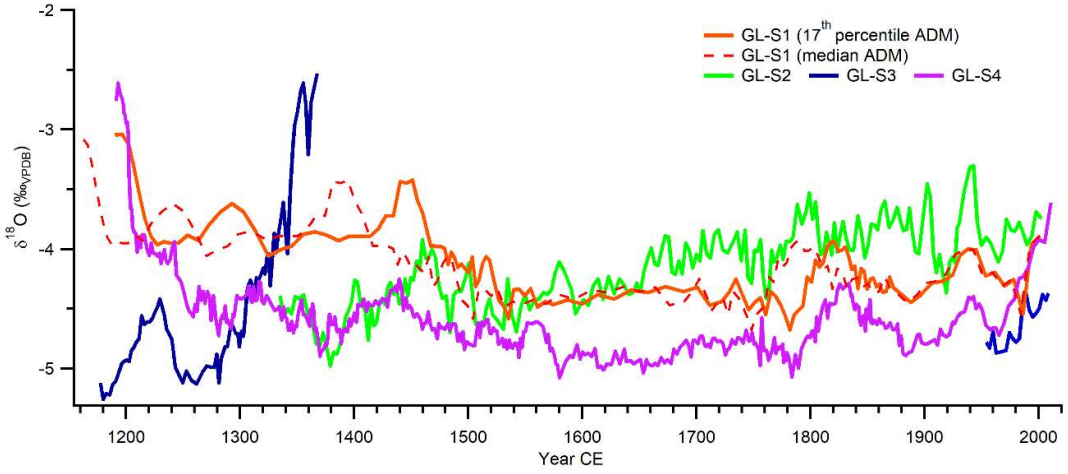


**Supplementary Figure 5:** Stalagmite $\delta^{18}O$ data shown with GL-S1 plotted using the 17$^{th}$ and 50$^{th}$ percentile U/Th age-depth models. GL-S1 $\delta^{18}O$ plotted on the 17$^{th}$ percentile ADM closely follows GL-S4 $\delta^{18}O$. GL-S4 chronology is based on laminae counting. A summary of the construction of each chronology is in Supplementary Table 4.

## Additional Supplementary References


1 Markowska, M. *et al.* Modern speleothem oxygen isotope hydroclimate records in water-limited SE Australia. *Geochim Cosmochim Ac* **270**, 431-448, https://doi.org/10.1016/j.gca.2019.12.007 (2020).

2 Frisia, S. & Borsato, A. in *Developments in Sedimentology* Vol. 61 (eds A. M. Alonso-Zarza & L. H. Tanner) 269-318 (Elsevier, 2010).

3 Mickler, P. J., Stern, L. A. & Banner, J. L. Large kinetic isotope effects in modern speleothems. *Geological Society Of America Bulletin* **118**, 65-81 (2006).

4 Mahmud, K., Mariethoz, G., Treble, P. C. & Baker, A. Terrestrial LiDAR survey and morphological analysis to identify infiltration properties in the Tamala Limestone, Western Australia. *IEEE Journal of Selected Topics in Applied Earth Observations and Remote Sensing* **8**, 4871-4881, doi:10.1109/JSTARS.2015.2451088 (2015).

5 Gat, J. R. Oxygen and Hydrogen Isotopes in the Hydrologic Cycle. *Annual Review of Earth and Planetary Sciences* **24**, 225-262, doi:10.1146/annurev.earth.24.1.225 (1996).

6 Horita, J. & Wesolowski, D. J. Liquid-vapor fractionation of oxygen and hydrogen isotopes of water from the freezing to the critical temperature. *Geochim Cosmochim Ac* **58**, 3425-3437 (1994).

7 Mahmud, K. *et al.* Estimation of deep infiltration in unsaturated limestone environments using cave LiDAR and drip count data. *Hydrological and Earth System Sciences* **20**, 359-373, doi:10.5194/hess-20-359-2016 (2016).

8 Treble, P. C. *et al.* An isotopic and modelling study of flow paths and storage in Quaternary calcarenite, SW Australia; implications for speleothem paleoclimate records. *Quaternary Science Reviews* **64**, 90-103, doi:10.1016/J.Quascirev.2012.12.015 (2013).

9 Markowska, M. *et al.* Modelling the $^{14}C$ bomb-pulse in young speleothems using a soil carbon continuum model. *Geochim Cosmochim Ac* **261**, 342-367, https://doi.org/10.1016/j.gca.2019.04.029 (2019).

10 Baker, A. *et al.* The Properties of Annually Laminated Stalagmites-A Global Synthesis. **59**, e2020RG000722, https://doi.org/10.1029/2020RG000722 (2021).